Airborne methane remote measurements reveal heavy-tail flux distribution in Four Corners region

Christian Frankenberg[a,b,1], Andrew K. Thorpe[b], David R. Thompson[b], Glynn Hulley[b], Eric Adam Kort[c], Nick Vance[b], Jakob Borchardt[d], Thomas Krings[d], Konstantin Gerilowski[d], Colm Sweeney[e,f], Stephen Conley[g,h], Brian D. Bue[b], Andrew D. Aubrey[b], Simon Hook[b], and Robert O. Green[b]

[a]Division of Geology and Planetary Sciences, California Institute of Technology, Pasadena, CA 91125; [b]Jet Propulsion Laboratory, California Institute of Technology, Pasadena, CA 91109; [c]Department of Climate and Space Sciences and Engineering, University of Michigan, Ann Arbor, MI 48109; [d]Institute of Environmental Physics, University of Bremen, 28334 Bremen, Germany; [e]Cooperative Institute for Research in Environmental Sciences, University of Colorado-Boulder, Boulder, CO 80309; [f]Global Monitoring Division, Earth System Research Laboratory, National Oceanic and Atmospheric Administration, Boulder, CO 80305; [g]Scientific Aviation, Boulder, CO 80301; and [h]Department of Land, Air, and Water Resources, University of California, Davis, CA 95616

Edited by Gregory P. Asner, Carnegie Institution for Science, Stanford, CA, and approved June 17, 2016 (received for review April 10, 2016)

Methane (CH_4) impacts climate as the second strongest anthropogenic greenhouse gas and air quality by influencing tropospheric ozone levels. Space-based observations have identified the Four Corners region in the Southwest United States as an area of large CH_4 enhancements. We conducted an airborne campaign in Four Corners during April 2015 with the next-generation Airborne Visible/Infrared Imaging Spectrometer (near-infrared) and Hyperspectral Thermal Emission Spectrometer (thermal infrared) imaging spectrometers to better understand the source of methane by measuring methane plumes at 1- to 3-m spatial resolution. Our analysis detected more than 250 individual methane plumes from fossil fuel harvesting, processing, and distributing infrastructures, spanning an emission range from the detection limit ∼ 2 kg/h to 5 kg/h through ∼ 5,000 kg/h. Observed sources include gas processing facilities, storage tanks, pipeline leaks, and well pads, as well as a coal mine venting shaft. Overall, plume enhancements and inferred fluxes follow a lognormal distribution, with the top 10% emitters contributing 49 to 66% to the inferred total point source flux of 0.23 Tg/y to 0.39 Tg/y. With the observed confirmation of a lognormal emission distribution, this airborne observing strategy and its ability to locate previously unknown point sources in real time provides an efficient and effective method to identify and mitigate major emissions contributors over a wide geographic area. With improved instrumentation, this capability scales to spaceborne applications [Thompson DR, et al. (2016) *Geophys Res Lett* 43(12):6571–6578]. Further illustration of this potential is demonstrated with two detected, confirmed, and repaired pipeline leaks during the campaign.

methane | Four Corners | remote sensing | heavy-tail

Global spaceborne measurements of methane with the Scanning Imaging Absorption Spectrometer for Atmospheric Chartography (SCIAMACHY) instrument (1) revealed a methane anomaly in the Four Corners region, with an estimated regional emission of 0.59 Tg/y (2). This study explores the role of point sources that supposedly drive the regional enhancement throughout the San Juan Basin in Four Corners.

The San Juan Basin is primarily a natural gas production area, mostly from coal bed methane and shale formations. More than 20,000 oil and gas wells operate in the basin, and, for 2009, the US Energy Information Administration reported an overall annual gas production of 1.3 trillion cubic feet, equivalent to 19.2 Tg CH_4/y.

To estimate methane emissions from oil and gas facilities, the Environmental Protection Agency uses a process-based approach that assumes a normal distribution of emissions for each process used in extraction, processing, and distribution. In reality, the flux distribution can be heavily skewed, resulting in a heavy-tailed distribution. This suggests that a relatively small percent of the sources in a given field may dominate the overall budget. The role of heavy-tail distributions has been discussed as a possible reason for underestimated methane emissions in bottom-up inventories (3–5). Although the heavy-tailed distribution makes it more difficult to estimate emissions using a process-based (or bottom up) approach, it suggests that mitigation of field-wide emissions such as those estimated for Four Corners will be less costly because it only requires identifying and fixing a few emitters.

However, evaluating the distribution and role of point sources in large geographical areas with limited road access is too time-consuming without prior knowledge of suspected locations. We conducted an intensive airborne campaign in April 2015 to overcome this shortcoming and directly measure the source distribution, identify strong emitters, and provide real-time feedback to ground teams. We flew two NASA/Jet Propulsion Laboratory airborne imaging spectrometers, namely, the next-generation Airborne Visible/Infrared Imaging Spectrometer (AVIRIS-NG) (6) and the Hyperspectral Thermal Emission Spectrometer (HyTES).

Recent studies have shown that both can retrieve methane quantitatively using methane absorption features in the shortwave infrared around 2.3 μm [AVIRIS-NG (7, 8)] and in the thermal infrared around 7.65 μm [HyTES (ref. 9 or refs. 10 and 11)]. Here, we report on the experiment design as well results from both instruments, having successfully identified more than 250 individual point sources, for which quantitative flux estimates are derived.

Significance

Fugitive methane emissions are thought to often exhibit a heavy-tail distribution (more high-emission sources than expected in a normal distribution), and thus efficient mitigation is possible if we locate the strongest emitters. Here we demonstrate airborne remote measurements of methane plumes at 1- to 3-m ground resolution over the Four Corners region. We identified more than 250 point sources, whose emissions followed a lognormal distribution, a heavy-tail characteristic. The top 10% of emitters explain about half of the total observed point source contribution and ∼1/4 the total basin emissions. This work demonstrates the capability of real-time airborne imaging spectroscopy to perform detection and categorization of methane point sources in extended geographical areas with immediate input for emissions abatement.

Author contributions: C.F. designed research; C.F., A.K.T., D.R.T., E.A.K., J.B., T.K., K.G., C.S., A.D.A., S.H., and R.O.G. performed research; C.F., A.K.T., D.R.T., G.H., N.V., J.B., T.K., S.C., and B.D.B. analyzed data; and C.F., A.K.T., and E.A.K. wrote the paper.

The authors declare no conflict of interest.

This article is a PNAS Direct Submission.

Freely available online through the PNAS open access option.

[1]To whom correspondence should be addressed. Email: cfranken@caltech.edu.

This article contains supporting information online at www.pnas.org/lookup/suppl/doi:10.1073/pnas.1605617113/-/DCSupplemental.

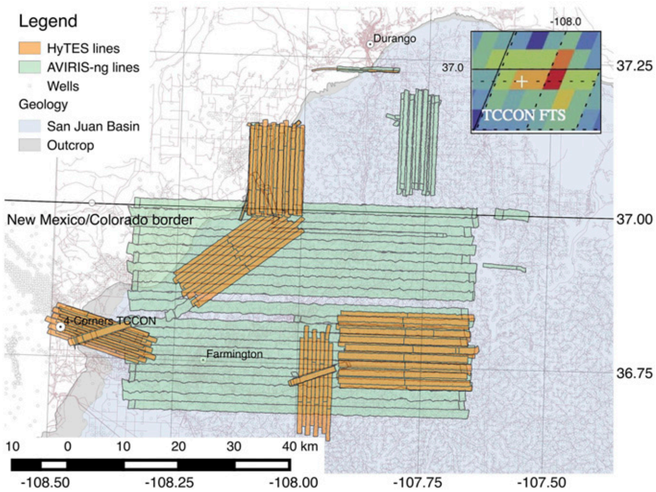

Fig. 1. Airborne Experiment overview of the Four Corners area. The ground projections of individual airborne imagery are shown for both instruments. (*Inset*) The previous SCIAMACHY enhancements (2).

Experiment Design

The overarching strategy was to map most of the identified methane hotspot in Four Corners (2), covering an area of around 80 × 40 km^2. Fig. 1 provides an overview of the study area, indicating a focus on the northwestern part of the San Juan Basin and its outcrop area toward the west (coal mine) and north. We covered a large box between 36.66 to 37°N and 107.66 to 108.33°W, east of the Total Carbon Column Observing Network (TCCON) Four Corners site (12), which operated until March 2014. Additional flight lines covered the coal mine a few kilometers east of the TCCON site as well as the natural outcrop area and smaller areas in Colorado near our home base at the Durango airport.

In most cases, AVIRIS-NG flew at about 3 km above ground level (AGL), allowing a wider swath to map larger areas, whereas HyTES flew at 1 km AGL, leveraging the enhanced methane sensitivities of the thermal band when flying low. For AVIRIS-NG, we used a recently developed real-time detection algorithm (13), enabling us to both identify and geolocate methane plumes in flight. This software allowed us to (*i*) convey plume locations to the ground-based teams for follow-up investigations and (*ii*) perform spontaneous repeat overflights or provide guidance for additional flight lines in the following days. For some of the ambiguous findings, ground-based verification could thus be performed during the flight campaign, often on the same day.

Results

HyTES. For HyTES, we used a Clutter Matched Filter Approach (CMF) (*Materials and Methods*) to isolate methane plumes. Some examples are shown in Fig. 2, ranging from a small plume to one emanating from a storage tank, extending almost 1 km.

Even though HyTES didn't have a real-time retrieval capability during the campaign, some locations could be corroborated by our ground team if the plumes had been detected by AVIRIS-NG as well. The large plume in Fig. 2, cut off by the end of the HyTES swath at the northern edge, is one example, for which we could trace down the origin to a leaking storage tank (Movie S1). In the remainder of this manuscript, we focus on the large-scale AVIRIS-NG survey and quantitative upscaling of total flux rates.

AVIRIS-NG. For AVIRIS-NG, we used a linearized matched filter technique for the entire dataset as well as using the Iterative Maximum a Posteriori Differential Optical Absorption Spectroscopy (IMAP-DOAS) method for selected scenes (*Materials and Methods*). Both methods derive column methane enhancements, expressed in ppm × meters, representing the plume methane mixing ratio if the plume was 1 m thick. In total, we identified 245 individual point sources and computed an integrated methane enhancement (IME) for each, integrating the total mass of excess methane within the plume structure (*Materials and Methods*).

Here, we use IME as a proxy for the total methane flux from a point source, as emissions and methane enhancements are linearly related at constant wind speed, and full plume inversions for more than 250 point sources are not yet feasible. We tested the approach against both Gaussian Integral inversions (*Materials and Methods*, *Supporting Information*, and Figs. S1–S5) and flux estimates derived using a mass balance approach with in situ measurements obtained during circling known sources at different height levels (similar to ref. 14). For the former, we selected individual plumes of variable size and used Gaussian Integral modeling to invert the flux based on the remotely sensed plume structure and magnitude. For the latter, we performed joint overflights on 22 April, targeting three previously identified methane sources of variable strength. While circular patterns were flown around the respective site for about 20 min to 30 min using an aircraft equipped with in situ methane measurements, AVIRIS-NG observed the scene three to four times.

Fig. 2. HyTES methane plume examples for a small, intermediate, and large plume (left to right), related to well pads as well as a storage tank, positively identified by the ground crew (Movie S1). Note the scale difference of the pictures.

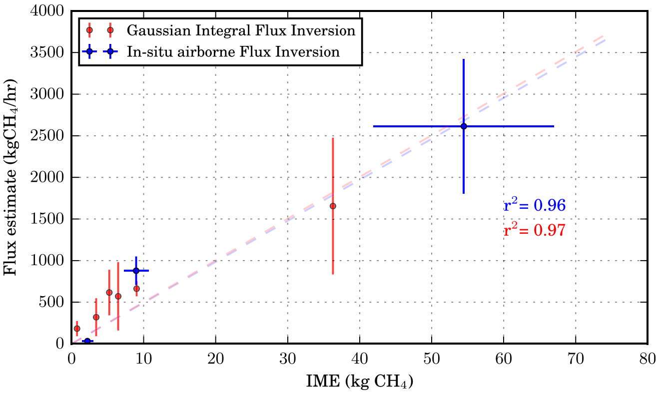

Fig. 3. IME (*x* axis) against inverted methane fluxes (*y* axis) using two different datasets and techniques. The scaling factor is derived using three local sources estimated using in situ airborne sampling circling the location at different altitudes (blue) as well as Gaussian integration methods using the observed plumes from AVIRIS-NG (red), for which an average wind speed of 2 m/s was assumed. The average of the slopes has been used for upscaling, and the high r^2 is driven by the largest fluxes.

The results are shown in Fig. 3, with very high correlations for both comparisons. In the following, we use the averaged slope between the two methods to estimate methane fluxes from IME. Owing to variable meteorological conditions in the complex terrain, errors on individual estimates can be high. In a statistical sense, many of these errors will cancel out in aggregates, however, as variable conditions will lead to both overestimations and underestimations. In the absence of direct wind measurements for each of the >200 plumes, we have to rely on statistical approaches to characterize the area quantitatively. In addition, many emissions, such as liquid unloading events (15, 16), are transient and more variable in time than our actual measurement error during a specific overpass. Performing a large-scale survey with AVIRIS-NG provides a representative statistical distribution if individual events are randomly distributed in time. It should be noted that the Gaussian Inversions assumed 2-m/s wind speed, and the three direct aircraft inversions were performed at 2- to 3-m/s wind speed, whereas the average wind speed for all aircraft in situ inversions was 4 m/s. Our upscaling is thus more likely to be conservative rather than an overestimate.

We find that the flux rates follow a lognormal distribution, as shown in Fig. 4 for all 245 plumes detected by AVIRIS-NG. Other studies have discussed and observed this type of distribution (3, 4), but here this emissions distribution was observed for a range of point sources over a large geographic scale within 1 wk. Fig. 4 also shows plume examples for a diverse range of estimated fluxes, as indicated by numbered vertical gray lines in the flux distribution plot. Even though our quantitative upscaling may be prone to large individual errors, especially due to wind variation, the lognormal distribution would not be strongly affected by this, thus robustly summarizing the overall source distribution using actual data with full spatial coverage across a wide geographical area.

A few of the plumes warrant a more detailed discussion. Plume #2 represents one example where the AVIRIS-NG real-time methane retrieval was invaluable. As can be seen, the methane plume appears unrelated to any gas processing facility and might have been considered spurious without corroboration. In this case, however, the ground team could follow up, and they positively identified a pipeline leak (Movie S2) and subsequently reported to the operating company, which shut down the pipeline and commenced repair the day after. The same happened at another location during the campaign, with ground confirmation and subsequent reporting to the pipeline operator. Two additional potential locations (Fig. S6) were identified in March 2016 while preparing this manuscript and have been reported to the respective state authorities. These have been subsequently confirmed as a pipeline leak and natural seep.

Plume #4, with a flux rate around 100 kg/h, was also followed up by the ground team and could be traced to a hatch in an underground storage tank (Movie S3). Plume #6, with an estimated flux rate of ~1,600 kg/h, is a coal mine venting shaft, about 7.5 km to the east of the TCCON station. It represents a strong source, which has been sampled by the in situ aircraft multiple times, with direct flux estimates ranging from 360 kg/h to 2,800 kg/h, in line with our estimate. Example #7 has been observed multiple times as well, and its origin is unclear, as the site was inaccessible to the ground team. The estimated flux is slightly higher than the venting shaft and is caused by multiple strong plumes, presumably emanating from newly built gas production and processing facilities. This site is only 3.5 km to the east of the coal mine venting shaft and is one example where the in situ aircraft suspected an additional strong source but was unable to trace it back to a specific location. Even without quantitative methane retrievals, the mere detection of individual plumes and the capability to geolocate strong sources to within a few meters is invaluable for source attribution and design of ground-based studies.

Plume #8 has to be treated differently, even though it represents the highest observed flux rate, estimated at 7,500 kg/h. It was observed at the gas processing facility near the Durango airport in Colorado. As Durango was our base, we overflew this site multiple times, usually without plume detection. On one particular occasion, a very strong plume was found, even though the swath didn't cover the entire facility (swath edge indicated by thin white line in Fig. 4). Knowing that this is a sporadic but very large source renders average flux estimation difficult without specific knowledge of industry practices and what caused that specific incident.

Apart from this large flux from plume #8, the entire dataset constituting the flux distribution in Fig. 4 is based on the regular survey flights only and thus excludes multiple overflights. Even though individual flux rates can vary dramatically in time (as evidenced by plume #8), a large-scale survey should provide a statistically representative sample, particularly when such a large number of sources are sampled in the survey. Repeated mapping of the entire area would be invaluable to assess source types and discriminate permanent and transient fluxes. In the following analysis, we divided the estimated flux from plume #8 by a factor of 4 to account for the number of multiple overpasses. Summing up all fluxes yields a regional total of ~0.3 Tg/y, explaining about half of the previously reported total of 0.59 Tg/y (2). Owing to the complexities of the retrievals and the upscaling and intermittency of sources, a full theoretical error propagation of all terms into a final regional flux estimate is not necessarily meaningful. Hence, we performed a nonparametric bootstrap analysis of the 245 plumes, resulting in a 95% confidence interval of 0.23 Tg/y to 0.39 Tg/y.

Flux Distribution. The lognormal behavior directly implies a heavy-tail distribution in absolute fluxes. The aerial surveys directly observed the lognormal distribution in a bottom-up survey. The cumulative distribution function shows that the biggest 10% of all plumes contributes about 60% to the inferred point source flux (Fig. 5). Using a parametric bootstrap method, the range of explained fluxes at the 10 percentile level ranges from 35 to 60% of the overall point source flux.

The nature of the lognormal distribution explains the large randomness of this explained fraction, as the sample size of large emitters is very low and thus largely variable using random draws. Another important aspect is the behavior of the low-flux tail of the lognormal distribution. It might be argued that emissions below our detection threshold of 2 kg/h to 5 kg/h [depending on wind speed (8)] might contribute substantially to the total flux. However, the theoretical lognormal curve, which would not be cut

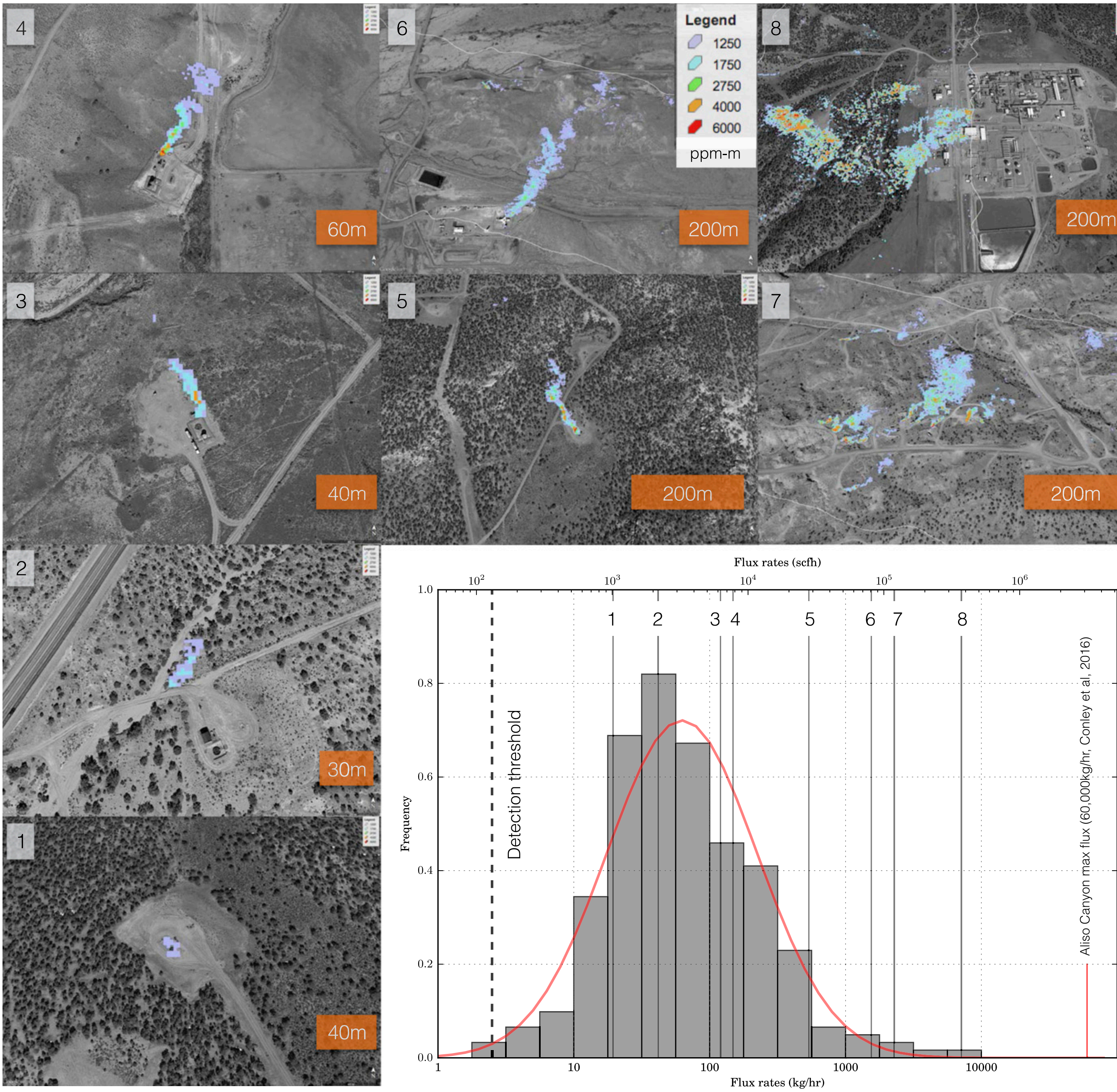

Fig. 4. Flux distribution of all 245 plumes observed by AVIRIS-NG with individual examples spanning the entire range of fluxes from low to high. Examples include well pads (*1* and *5*), a confirmed pipeline leak (*2*), storage tanks (*3* and *4*), gas processing facilities (*8*), a coal mine venting shaft (*6*), and a cluster of strong sources near a well completion site (*7*). The detection threshold is based on controlled release experiments performed at the Rocky Mountain Operating Test Facility in Wyoming (*8*). The fitted lognormal distribution has a mean of $10^{1.75}$ and a 1σ of 0.55. For comparison, the unique Aliso Canyon blowout is depicted as a red line, corresponding to a maximum flux rate of 60,000 kg/h.

off below the threshold, shows negligible contributions from low fluxes as well. A bimodal distribution with a peak at flux rates well below our detection would need to exist if small fluxes were to contribute substantially to the regional flux total. Airborne remote sensing appears to be an effective way of identifying the biggest point sources in large geographical areas and thus efficiently mitigating avoidable emissions such as pipeline leaks or faulty storage tanks.

Discussion and Conclusion

We performed a large-scale aerial survey in New Mexico and Colorado to map methane plumes within a previously discovered large-scale methane hotspot. For this study, satellite-based observations at the 60 × 30 km scale guided this detailed follow-up study with imaging spectrometers and 1- to 3-m spatial resolution. A real-time methane retrieval further allowed us to provide exact locations of individual points of interest to a ground team, which could follow up with thermal infrared videos, narrowing down the exact cause for various plumes, with most prominent examples covering leaking storage tanks and pipeline leaks. Using a simple linear scaling of integrated excess methane, we derived estimates of methane flux rates, ranging from a few kilograms per hour to several thousand kilograms per hour. Fig. 6

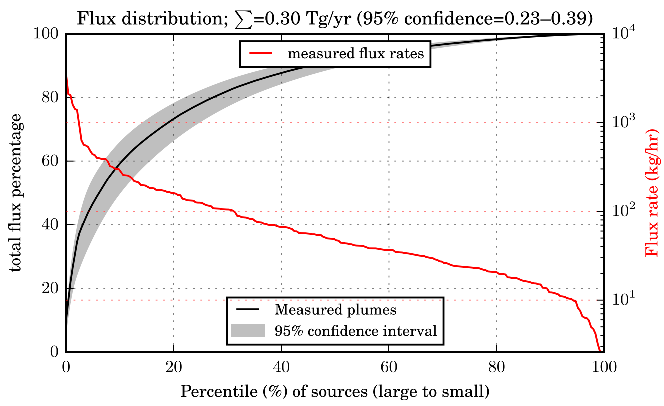

Fig. 5. Black line denotes cumulative distribution function of summed fluxes against flux percentiles (in descending order). Red line denotes corresponding flux rates at the respective percentile. The gray area shows the 95% confidence interval of the distribution, using a nonparametric bootstrap method.

provides an overview of all detected point sources (see *Supporting Information* for details).

Our upscaled flux estimate of all point sources ranges from 0.23 Tg/y to 0.39 Tg/y, explaining 39 to 66% of the total regional emissions determined for 2003 through 2009 (2). This finding confirms earlier assumptions that most of the enhanced methane is related to natural gas extraction as well as coal mining but also that there is not a single source explaining most enhancements. The observed lognormal source distribution further implies that small sources below 1 kg/h contribute very little to the total flux rate. However, it should be noted that our snapshots in time might only catch periodic emissions that exceed our detection threshold at the time of overpass, resulting in an overestimate for these locations, while others are missed. Imaging thousands of wells across the area should nevertheless provide a statistical sampling and thus a nonbiased regional average. In the future, repeat overflights can further discriminate transient from persistent sources and thereby greatly help to evaluate source mitigation potentials across large geographic areas.

Our analysis shows that strong emitters dominate the regional budget, with presumably lower marginal cost for emissions reductions. We have also demonstrated the ability to quantify and identify both small and large point source emissions widely spread over inaccessible geographic areas. Airborne remote measurements, combined with in situ sensing, could thus provide a path forward toward effective methane emission (monitoring) mitigation strategies. A dedicated sensor with increased sensitivity through higher spectral resolution would also reduce spurious signals (17) and enable efficient automation of the retrieval and plume detection chain, similar to current satellite retrieval algorithms.

Materials and Methods

AVIRIS-NG Methane Retrievals. AVIRIS-NG measures reflected solar radiation between 0.35 μm and 2.5 μm with 5-nm spectral resolution and sampling. Here, we used two related CH_4 retrieval algorithms based on absorption spectroscopy (7, 13), namely, (*i*) IMAP-DOAS and (*ii*) a linearized matched filter technique.

The IMAP method was originally developed for use with the SCIAMACHY satellite instrument (18) and has been modified for use with imaging spectrometers AVIRIS and AVIRIS-NG (7). Using a nonlinear iterative minimization of the differences between modeled and measured radiance, we quantitatively retrieve the excess methane abundances below the aircraft.

The real-time CH_4 retrieval exploits a linearized matched filter strategy described previously in ref. 13. We model the background radiance spectra as a multivariate Gaussian having mean μ and covariance Σ, and estimate its parameters using the image data in the appropriate pushbroom cross-track location. The matched filter tests the null background case H_0 against the alternative H_1 in which the background undergoes a linear perturbation by a target signal **t**,

$$H_0 : \mathbf{x} \sim \mathcal{N}(\mu, \Sigma) \quad H_1 : \mathbf{x} \sim \mathcal{N}(\mu + \alpha\mathbf{t}, \Sigma)\,. \qquad [1]$$

Here α represents a scaling of the perturbing signal. The optimal discriminant is the classical matched filter $\hat{\alpha}(\mathbf{x})$. It estimates α using a noise-whitened dot product. This takes the form

$$\hat{\alpha}(\mathbf{x}) = \frac{(\mathbf{x}-\mu)^T\Sigma^{-1}\mathbf{t}}{\mathbf{t}^T\Sigma^{-1}\mathbf{t}}. \qquad [2]$$

For our real-time retrieval, we calculate the target signature as the change in radiance units of the background caused by adding a unit mixing ratio length of CH_4 absorption. The additional absorption acts as a thin Beer–Lambert attenuation of the background μ. Specifically, our target signature is the partial derivative of measured radiance with respect to a change in absorption path length ℓ by an optically thin absorbing layer of CH_4. At $\ell = 0$, we have

$$\mathbf{t} = \frac{\partial \mathbf{x}}{\partial \ell} = -\mu e^{-\kappa\ell}\kappa = -\mu\kappa, \qquad [3]$$

where κ represents the unit absorption coefficient and μ is the mean radiance as before. The detected quantity $\hat{\alpha}(\mathbf{x})$ is a mixing ratio length in units of ppb × km representing the thickness and concentration within a volume of equivalent absorption.

For both retrieval techniques, we compute methane enhancements in parts per million per meter, which is equivalent to an excess methane concentration in parts per million if the layer is 1 m thick (i.e., directly equivalent to parts per billion per kilometer). At a scale height of about 8 km, the total column averaged excess mixing ratio XCH_4 would be about 0.000125 times the excess in parts per million per meter. For example, 1,000 ppm/m is equivalent to an XCH_4 enhancement of 125 ppb.

HyTES Methane Retrievals. HyTES has sufficient spectral information in the 7.4- to 12-μm region (256 bands) to resolve the spectral absorption signatures of a variety of different atmospheric chemical species including CH_4, NO_2, NH_3, SO_2, N_2O, and H_2S. An in-scene atmospheric technique is first used to remove the background attenuation from the intervening atmosphere and then find evidence of the gas target signature that is assumed to be linearly superimposed on the background radiance data. A CMF (19–21) is then used to generate a weighting function based on a given specific target gas signature extracted from the HITRAN high-resolution transmission molecular absorption database. The weighting function is superimposed on the observed hyperspectral data to generate a CMF image in which the intensity of the image correlates with the presence of the desired gas signature.

In addition to the CMF detection algorithm, a HyTES CH_4 concentration retrieval algorithm was developed and adapted from the algorithm used for

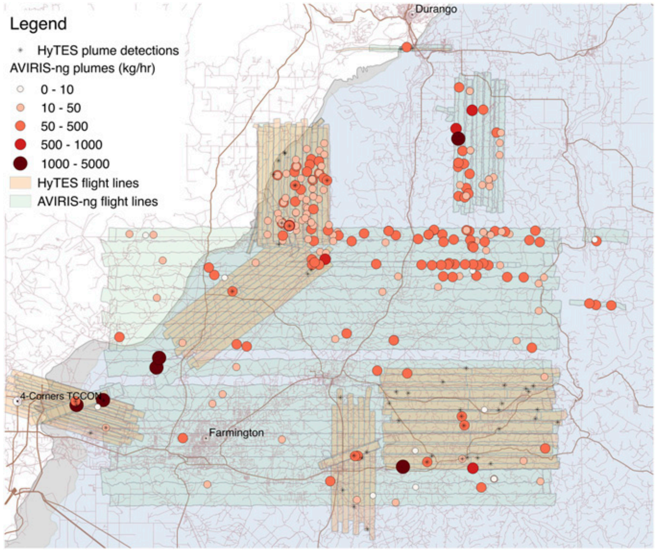

Fig. 6. Map of covered areas and detected point sources by HyTES (stars) and AVIRIS-NG (red dots with estimated flux rates color-coded).

retrieving trace gases from the Tropospheric Emission Spectrometer (TES) onboard the Aura satellite. Using HyTES radiance spectra in the 7.5- to 9.2-μm range, the HyTES-TES quantitative algorithm has been used to quantify methane concentrations with a total error of ~20% using uncertainties determined primarily from instrument noise and spectral interferences from air temperature, surface emissivity, and atmospheric water vapor (22).

Methane Flux Inversion. Emission rates from the remote sensing column information were obtained using a mass balance approach similar to (23, 24)

$$F = \int \int_S V\, \vec{u} \cdot \vec{n}\, dS$$
$$\approx \vec{u} \cdot \vec{n} \sum_i V_i\, \Delta S_i,$$

where V denotes the vertical column of CH_4, $\vec{u}$ is the wind. and $\vec{n}$ is the normal vector on the boundary S. The integral is evaluated in its discretized form on a straight cross-section with segments of length $\Delta S = 1$ m and interpolated vertical column information V_i.

For each target, multiple cross-sections orthogonal to the wind direction were defined at different distances to the analyzed sources. Thereby the background was determined via a linear background fit over regions in the cross-section outside the plume. Typically, each flank comprises about 10 to 20% of total data points in a track. About 15 to 100 individual cross-sections were then averaged for a mean emission rate. Examples are shown in *Supporting Information*.

IME. We use IME, a measure of the total excess mass of observed methane, as a surrogate for fluxes of all identified plumes. We use a segmentation technique to isolate the methane plumes with an XCH_4 minimum threshold of 200-ppm/m enhancements and subsequent summation of all pixels multiplied with the surface area S of an individual measurement i,

$$IME = k \sum_{i=0}^{n} XCH_4(i) \cdot S(i),$$

with a constant factor k to convert a methane volume into grams of CH_4. Observed excess IME ranged from 100 g to about 100 kg.

Thermal Infrared Videos: Movies S1–S3. A Xenics Onca-VLWIR-MCT-384 thermal imaging camera was used to identify plumes as part of ground surveys. This instrument has a 384 × 288 pixel resolution and HgCdTe detector sensitive between 7.7 μm and 11.5 μm. For this study, a Spectrogon optical filter centered at 7.746 μm was used as a digital filter applied to a contiguous spectrometer output to match either an absorption or emission response of methane, creating contrast between methane plumes and the background.

ACKNOWLEDGMENTS. We thank the AVIRIS-NG flight and instrument teams, including Michael Eastwood, Sarah Lundeen, Scott Nolte, Mark Helmlinger, and Betina Pavri. Didier Keymeulen and Joseph Boardman assisted with the real-time system. We also thank the HyTES flight and instrument teams, including Bjorn Eng, Jonathan Mihaly, Seth Chazanoff, and Bill Johnson. We thank the organizers and all the participants in the TOPDOWN campaign for the fruitful collaboration. We thank NASA Headquarters, in particular Jack Kaye, for funding this flight campaign, which augmented the overall Twin Otter Projects Defining Oil/Gas Well Emissions (TOPDOWN) campaign. J.B., T.K., and K.G. were funded by the state of Bremen and University of Bremen. E.A.K. and C.S. were supported, in part, by the National Oceanic and Atmospheric Administration AC4 program under Grant NA14OAR0110139.

1. Frankenberg C, et al. (2011) Global column-averaged methane mixing ratios from 2003 to 2009 as derived from SCIAMACHY: Trends and variability. *J Geophys Res* 116(D4): D04302.
2. Kort EA, et al. (2014) Four corners: The largest US methane anomaly viewed from space. *Geophys Res Lett* 41(19):6898–6903.
3. Brandt AR, et al. (2014) Methane leaks from North American natural gas systems. *Science* 343(6172):733–735.
4. Zavala-Araiza D, et al. (2015) Reconciling divergent estimates of oil and gas methane emissions. *Proc Natl Acad Sci USA* 112(51):15597–15602.
5. Lyon DR, et al. (2016) Aerial surveys of elevated hydrocarbon emissions from oil and gas production sites. *Environ Sci Technol* 50(9):4877–4886.
6. Green RO, et al. (1998) Imaging spectroscopy and the Airborne Visible/Infrared Imaging Spectrometer (AVIRIS). *Remote Sens Environ* 65(3):227–248.
7. Thorpe AK, Frankenberg C, Roberts D (2014) Retrieval techniques for airborne imaging of methane concentrations using high spatial and moderate spectral resolution: Application to AVIRIS. *Atmos Meas Tech* 7(2):491–506.
8. Thorpe AK, et al. (2016) Mapping methane concentrations from a controlled release experiment using the next generation Airborne Visible/Infrared Imaging Spectrometer (AVIRIS-NG). *Remote Sens Environ* 179:104–115.
9. Hulley GC, et al. (2016) High spatial resolution imaging of methane and other trace gases with the airborne Hyperspectral Thermal Emission Spectrometer (HyTES). *Atmos Meas Tech* 9(5):2393–2408.
10. Tratt DM, et al. (2014) Airborne visualization and quantification of discrete methane sources in the environment. *Remote Sens Environ* 154:74–88.
11. Galfalk M, Olofsson G, Crill P, Bastviken D (2015) Making methane visible. *Nat Clim Change* 6(4):426–430.
12. Lindenmaier R, et al. (2014) Multiscale observations of CO_2, $^{13}CO_2$, and pollutants at Four Corners for emission verification and attribution. *Proc Natl Acad Sci USA* 111(23): 8386–8391.
13. Thompson D, et al. (2015) Real-time remote detection and measurement for airborne imaging spectroscopy: A case study with methane. *Atmos Meas Tech* 8(10):4383–4397.
14. Conley S, et al. (2016) Methane emissions from the 2015 Aliso Canyon blowout in Los Angeles, CA. *Science* 351(6279):1317–1320.
15. Allen DT, et al. (2013) Measurements of methane emissions at natural gas production sites in the United States. *Proc Natl Acad Sci USA* 110(44):17768–17773.
16. Allen DT, et al. (2015) Methane emissions from process equipment at natural gas production sites in the United States: Liquid unloadings. *Environ Sci Technol* 49(1): 641–648.
17. Thorpe AK, et al. (2016) The Airborne Methane Plume Spectrometer (AMPS): Quantitative imaging of methane plumes in real time. *Conf Proc IEEE,* in press.
18. Frankenberg C, Platt U, Wagner T (2005) Iterative maximum a posteriori (IMAP)-DOAS for retrieval of strongly absorbing trace gases: Model studies for CH_4 and CO_2 retrieval from near infrared spectra of SCIAMACHY onboard ENVISAT. *Atmos Chem Phys* 5(1):9–22.
19. Funk CC, Theiler J, Roberts DA, Borel CC (2001) Clustering to improve matched filter detection of weak gas plumes in hyperspectral thermal imagery. *IEEE Trans Geosci Remote Sens* 39(7):1410–1420.
20. Theiler J, Foy BR (2006) Effect of signal contamination in matched-filter detection of the signal on a cluttered background. *IEEE Geosci Remote Sens Lett* 3(1):98–102.
21. Hulley GC, et al. (2016) High spatial resolution imaging of methane and other trace gases with the airborne Hyperspectral Thermal Emission Spectrometer (HyTES). *Atmos Meas Tech* 9(5):2393–2408.
22. Kuai L, et al. (2016) Characterization of anthropogenic methane plumes with the Hyperspectral Thermal Emission Spectrometer (HyTES): A retrieval method and error analysis. *Atmos Meas Tech Discuss* 2016:1–24.
23. Krings T, et al. (2011) Mamap—A new spectrometer system for column-averaged methane and carbon dioxide observations from aircraft: Retrieval algorithm and first inversions for point source emission rates. *Atmos Meas Tech* 4(9):1735–1758.
24. Krings T, et al. (2013) Quantification of methane emission rates from coal mine ventilation shafts using airborne remote sensing data. *Atmos Meas Tech* 6(1): 151–166.